PHOTONICS Research

Terahertz metasurface polarization detection employing vortex pattern recognition

CHENGLONG ZHENG,[1] [iD] JINGYU LIU,[2] HUI LI,[3] [iD] MENGGUANG WANG,[4,5] HUAPING ZANG,[1,6] [iD] YAN ZHANG,[2,7] [iD] AND JIANQUAN YAO[3]

[1]*Key Laboratory of Material Physics, Ministry of Education, School of Physics and Microelectronics, Zhengzhou University, Zhengzhou 450052, China*
[2]*Beijing Key Laboratory for Metamaterials and Devices, Key Laboratory of Terahertz Optoelectronics, Ministry of Education, and Beijing Advanced Innovation Center for Imaging Technology, Department of Physics, Capital Normal University, Beijing 100048, China*
[3]*Key Laboratory of Opto-Electronics Information Technology (Tianjin University), Ministry of Education, School of Precision Instruments and Opto-Electronics Engineering, Tianjin University, Tianjin 300072, China*
[4]*State Key Laboratory of Modern Optical Instrumentation, College of Optical Science and Engineering, Zhejiang University, Hangzhou 310027, China*
[5]*e-mail: wangmengguang@zju.edu.cn*
[6]*e-mail: zanghuaping@zzu.edu.cn*
[7]*e-mail: yzhang@mail.cnu.edu.cn*

The manipulation and detection of polarization states play a crucial role in the application of 6G terahertz communication. Nonetheless, the development of compact and versatile polarization detection devices capable of detecting arbitrary polarizations continues to be a challenging endeavor. Here, we demonstrate a terahertz polarization detection scheme by performing mode purity analysis and multidimensional analysis of the transmitted vortex field. The power of the proposed polarization recognition is verified by using three polarization trajectories, including linear polarizations, circular polarizations, and elliptical polarizations. Using the reconstructed complete polarization parameters, the detected polarization states are characterized using polarization ellipses, Poincaré sphere, and full-Stokes parameters. The experimental results validate the power of this scheme in polarization detection. This scheme holds promise for applications in polarization imaging and terahertz communication.   © 2023 Chinese Laser Press

https://doi.org/10.1364/PRJ.506746

1. INTRODUCTION

A metasurface is capable of finely modulating incident waves on a subwavelength scale, pixel by pixel, profiting from its remarkable capabilities of manipulating electromagnetic waves [1]. The range includes, but is not limited to, the frequency, amplitude, phase, and polarization of the electromagnetic waves [2,3]. This modulation implementation originated from the concept of introducing phase discontinuities at interfaces, proposed by Capasso's group in 2011 [1]. Based on such strategies, researchers have developed various functional devices [4–16]. In addition to achieving functions that traditional optics and diffractive optical elements can accomplish, a metasurface introduces more degrees of freedom for modulating the optical field. By adjusting the phase gradient at the interface, incident waves can be deflected in any desired direction, and the generation and control of multiple beams can be achieved [4,5]. Furthermore, it can be used for polarization conversion [6,7], holography [8,9], metalenses [10,11], vortex beams [12–14], and other functionalities, offering tremendous prospects for applications in imaging, communication, sensing, and other fields.

Vortex beams, which carry orbital angular momentum (OAM) during propagation, have been widely used in fields such as OAM communication, optical trapping, and edge-enhanced imaging [17–19]. There are various methods to generate such beams, including mode conversion, spiral phase plates, spiral zone plates, q-plates, and metasurfaces [19–22]. The topological charge of the generated vortex can be flexibly adjusted through designing the structure or phase profile of the element. In addition to generating and controlling a single vortex state, the orthogonality between vortex beams with different topological charges makes the superposition of multiple vortex modes useful in quantum science and communication [23,24]. Vortex superposition states can be utilized to record and transmit information.

Polarization, as a fundamental characteristic of electromagnetic waves, has important applications in communications, light–matter interactions, and so on. In addition to generating specific polarization beams, the detection of polarization is equally important. Methods such as Jones vector analysis, Stokes parameters, and Poincaré spheres can be used to characterize the polarization state of a light field. Traditional polarization detection methods involve the use of polarizers, waveplates, and the introduction of electro-optic crystals. In recent years, the development of metasurfaces has provided new solutions for polarization detection [24–27]. Zhang _et al._ demonstrated a polarimeter that can detect the incident angle and polarization state of incident light simultaneously [25]. Hu _et al._ experimentally demonstrated an ultracompact all-dielectric pixelated full-Stokes metasurface; each pixel consists of three linear polarizers and one circular polarizer with a single-layer planar structure [26]. Jiang _et al._ proposed a metallic waveguide array to measure the polarization state of continuous terahertz waves by measuring the phase difference and amplitude ratio of its two orthogonal components based on polarization-multiplexing vortex beams [27]. Liu _et al._ reported a bionic metasurface that can realize full-Stokes polarization imaging in a wide field of view [24]. However, current polarization detection schemes mostly rely on beam splitting and sub-region designs, which have larger dimensions and are not conducive to lightweight and integrated designs. Moreover, most of these schemes can only detect specific linear or circular polarization states.

In this work, we propose a novel terahertz polarization detection scheme. The scheme relies on a spin-decoupled all-dielectric metasurface that generates a pair of vortex beams with opposite topological charges based on the independent control of left-handed and right-handed circularly polarized incidences. Through the mode analysis of the transmitted field modulated by a metasurface, the parameters describing the incident polarization states are obtained completely, and then the incident polarization states are reconstructed by the full-Stokes parameters and Poincaré sphere. In order to verify the feasibility of such a polarization detection scheme, we simulate several polarization curves: the trajectory of the incident wave's polarization state following the meridian direction, the trajectory following the equatorial direction, and five arbitrarily selected elliptical polarization states. The experimental results also validate the power of this scheme in polarization detection. The device has great potential for the development of ultra-compact terahertz polarization detection devices, polarization imaging, and related applications.

2. DESIGN AND METHOD

In this paper, we employ a meticulous design of the metasurface's phase profile to effectively reconstruct the polarization state of the incident wave. This is achieved through a comprehensive analysis of the mode exhibited by the transmitted field. Figure 1 shows the schematic of the proposed all-dielectric metasurface for terahertz polarization detection. For arbitrarily polarized wave incidence (linearly polarized, circularly polarized, or elliptically polarized), the transmitted field will behave as a superposition of two vortices or as a single vortex state. We
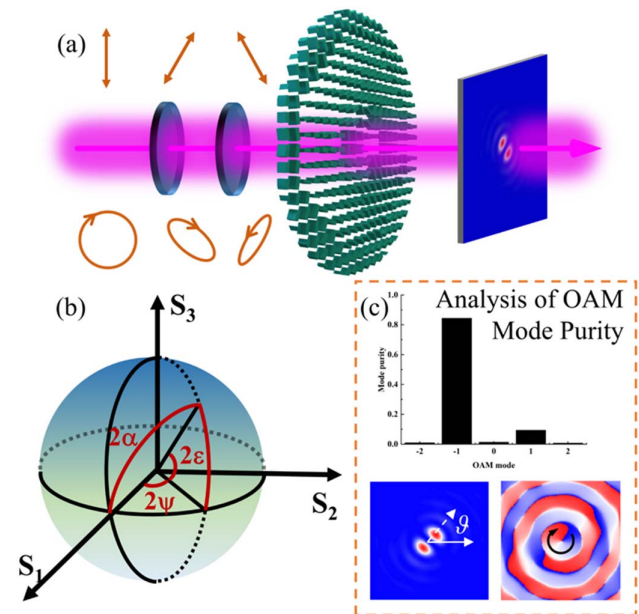

Fig. 1. Schematic of the proposed all-dielectric metasurface for terahertz polarization detection. (a) For arbitrarily polarized wave incidence, the incident polarization state can be obtained by analyzing the mode of the transmitted field. (b) Diagram of a Poincaré sphere; arbitrary polarization state on the spherical surface can be represented using three coordinates $(2\alpha, 2\psi, 2\varepsilon)$. (c) The mode analysis of the transmitted field mainly consists of three parts: first, the decomposition of the mode purity of the transmitted vortex field; second, the orientation angle of the transmitted x-polarized field; third, the phase distribution of the transmitted x-polarized component.

take a comprehensive analysis of the transmitted field's mode (polarization, intensity, phase, etc.), allowing us to extract the complete polarization parameters of the incident field. Here, we use the Poincaré sphere as an example to characterize the polarization state of the incident field [Fig. 1(b)], requiring the parameters of angle of amplitude ratio α, azimuth angle ψ, and ellipticity angle ε. These parameters can also be used to reconstruct the full-Stokes parameters of the incident field. The mode analysis of the transmitted field mainly consists of three parts, as shown in Fig. 1(c). In the first part, the decomposition of the mode purity of the transmitted vortex field is performed, allowing us to obtain ellipticity angle ε. In the second part, we determine the orientation angle ϑ of the x-polarized component in the transmitted field, which is related to azimuth angle ψ. The third part involves extracting the incident field's handedness based on the phase distribution of the x-polarized component. Additionally, the angle of amplitude ratio α is related to ellipticity angle ε and azimuth angle ψ, and can be calculated based on the other two quantities. By utilizing these reconstructed parameters, the polarization state of the incident field can be described using the Poincaré sphere and full-Stokes parameters.

The metasurface polarization detection scheme proposed in this paper is based on independent control of left-handed and right-handed circularly polarized incidences. In order to achieve this goal, we employ the principle of spin-decoupling to design

this device [28,29]. By fully utilizing the degrees of freedom of propagation phase and geometric phase, we can arbitrarily design the phase profiles of left-handed and right-handed circularly polarized waves by designing the structural parameters (length l and width w) and rotation angle ϑ of the anisotropic meta-atoms [Fig. 2(a)]. When arranging the meta-atoms, the relationship between the phase responses and rotation angle of the meta-atoms under linear polarizations and the phase profiles of circular polarizations can be described by the following equations:

$$\varphi_{xx} = (\varphi_{LCP} + \varphi_{RCP})/2,$$
$$\varphi_{yy} = (\varphi_{LCP} + \varphi_{RCP})/2 - \pi,$$
$$\theta = (\varphi_{RCP} - \varphi_{LCP})/4. \tag{1}$$

The phase responses of the meta-atoms under linear polarizations can be flexibly changed by adjusting the structural parameters of the meta-atoms. The operation frequency for the designed metasurface is 0.9 THz. The period of the designed meta-atom is 150 μm, and the height of the silicon pillars is 200 μm. After a series of parameter sweeps, we have selected 15 meta-atoms that satisfy the conditions. And their phase differences under linear polarizations remain about 180°, with high polarization conversion efficiencies. Their transmission amplitudes and phase shifts of the selected meta-atoms under the *x*- and *y*-polarized incidences are shown in Fig. 2(b). According to the description of Eq. (1), the spatial diagram of the meta-atom library used to achieve spin-decoupling is given in Fig. 2(c). For each row of eight meta-atoms, they have the same phase shifts when the left-handed circularly polarized light is incident. When the incident wave is right-handed circularly polarized, their phase shifts increase at 45° intervals from left to right.
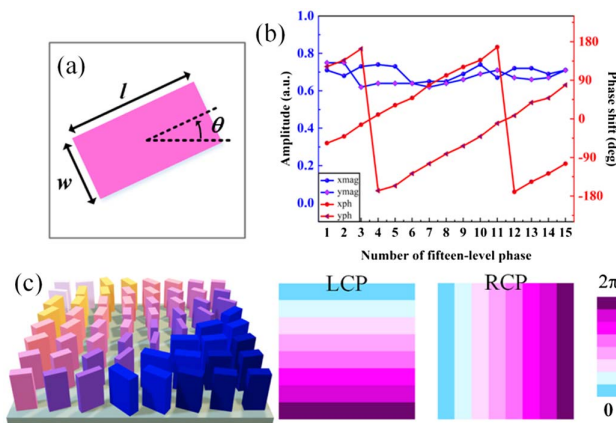

Fig. 2. Characterization of the used meta-atoms. (a) Diagram of the anisotropic rectangular pillar. (b) Simulated transmission amplitudes (blue) and phase shifts (red) of the selected 15 meta-atoms under the *x*- and *y*-polarized incidences. (c) Spatial diagram of the selected meta-atoms for realizing spin-decoupling. For each row of eight meta-atoms, they have the same phase shifts when the left-handed circularly polarized light is incident; for each column of eight meta-atoms, they have the same phase shifts when the incident wave is right-handed circularly polarized.

The key of this scheme is to generate two vortex beams with topological charges of +1 and −1, respectively, under left-handed and right-handed circularly polarized incidences. Then the relative intensities of the left-handed and right-handed circularly polarized components can be analyzed by investigating the purity of these two vortex modes. In order to achieve the generation of such vortex field on a single metasurface device, the theoretically required phase profiles can be expressed as

$$\varphi_{LR} = \frac{2\pi}{\lambda}\left(\sqrt{r^2 + f^2} - f\right) + \phi,$$
$$\varphi_{RL} = \frac{2\pi}{\lambda}\left(\sqrt{r^2 + f^2} - f\right) - \phi, \tag{2}$$

where φ_{LR} represents the phase profile of the transmitted right-handed circularly polarized component in response to left-handed circularly polarized incidence. The focal length f is set as $f = 4$ mm. After an arbitrarily polarized terahertz wave is incident on the device, the mode purities of the transmitted vortex field need to be decomposed, using the equations:

$$E(r,z) = \frac{1}{\sqrt{2\pi}}\sum_{l=-\infty}^{l=\infty} a_l(r,z)\exp(il\phi),$$
$$a_l(r,z) = \frac{1}{\sqrt{2\pi}}\int_0^{2\pi} E(r,z)\exp(-il\phi)\mathrm{d}\phi,$$
$$C_l = \int_0^\infty |a_l(r,z)|^2\, r\mathrm{d}r, \qquad P_l = C_l\Big/\sum_{l=-\infty}^{l=\infty} C_l, \tag{3}$$

where $E(r,z)$ is the transmitted vortex field, and C_l represents the energy of the vortex field $E(r,z)$ at harmonic $\exp(il\phi)$. Mode purities with topological charges of +1 and −1 are used in this paper to represent the relative intensities of the left-handed and right-handed circular polarizations in the incident wave. These two purities are denoted by M_{+1} and M_{-1}, respectively. According to the definition of Stokes parameters and the parameters of the polarization ellipse, it can be obtained that

$$\sin 2\varepsilon = \frac{S_3}{S_0} = \frac{M_{-1} - M_{+1}}{M_{-1} + M_{+1}}. \tag{4}$$

The ellipticity angle ε can be analyzed from the relative mode purity. For any polarization state, the Jones vector can be expressed as

$$J = \begin{bmatrix} \cos\alpha \\ \sin\alpha e^{i\delta} \end{bmatrix}, \tag{5}$$

where α represents the angle of amplitude ratio, δ is the phase difference of *x*- and *y*-polarizations. The transmitted field consisting of two vortex modes can be expressed as

$$E_t = E_L e^{i\phi}\begin{bmatrix} 1 \\ -i \end{bmatrix} + E_R e^{-i\phi}\begin{bmatrix} 1 \\ i \end{bmatrix}$$
$$= \frac{1}{2}(\cos\alpha + i\sin\alpha e^{i\delta})e^{i\phi}\begin{bmatrix} 1 \\ -i \end{bmatrix}$$
$$+ \frac{1}{2}(\cos\alpha - i\sin\alpha e^{i\delta})e^{-i\phi}\begin{bmatrix} 1 \\ i \end{bmatrix}, \tag{6}$$

where E_t represents the transmitted field, and E_L (E_R) represents the amplitude of left-handed (right-handed) circular polarization in the incident wave. The expression of the

transmitted x-polarization component can be decomposed from Eq. (6) as

$$E_x = \cos \alpha \cos \phi - \sin \alpha \sin \phi e^{i\delta}. \qquad (7)$$

Taking the phase difference $\delta = 0$ as an example, it can be obtained that E_x has the greatest intensity when $\phi = n\pi - \alpha$ (n is an integer). From the subsequent simulation results, the relationship between azimuth angle ψ and orientation angle ϑ is summarized as $\psi = \pi - \vartheta$.

The relationships of several parameters between the polarization ellipse and Poincaré sphere are as follows:

$$\cos 2\alpha = \cos 2\varepsilon \cos 2\psi,$$
$$\pm \sin 2\varepsilon = \sin 2\alpha \sin \delta. \qquad (8)$$

Using the known parameters of ellipticity angle ε and azimuth angle ψ, the remaining polarization parameters can be calculated, the polarization ellipse of the incident wave can be plotted, and the full-Stokes parameters can be obtained.

3. RESULTS AND DISCUSSION

Before applying this all-dielectric metasurface device to terahertz polarization detection, we simulate its transmission field. A vortex beam with a topological charge of $+1$ is generated in the transmitted right-handed circularly polarized channel under left-handed circularly polarized incidence (see Appendix A). For the right-handed circularly polarized incidence, there is a vortex beam with a topological charge of -1 generated in the other polarization channel. These results validate the functional design of the metasurface generating vortex fields, which lays a foundation for its application to the polarization detection of terahertz waves.

To verify the feasibility of the polarization detection scheme of this metasurface, three polarization trajectories will be used to demonstrate that. As the first part, the trajectory of the incident polarization state follows the meridian direction, transitioning from x-polarization to right-handed circular polarization, and then to y-polarization. For any polarization state on this trajectory, the incident polarization can be set by changing its axial ratio. In the actual simulations, 21 polarization states are selected along this trajectory for simulation (x-polarization, axial ratio $= 0.1, 0.2, \ldots, 0.9, 1, 1/0.9, \ldots, 1/0.1$, y-polarization). Seven sets of these results are shown in Figs. 3(a)–3(g). Their corresponding polarizations are x-polarization, axial ratio $= 0.3, 0.6, 1, 1/0.6, 1/0.3$, and y-polarization, respectively.

The first to third rows in Figs. 3(a)–3(g) correspond to the intensity distributions of the transmitted x-polarized components, the mode purity spectra of the transmitted vortex fields, and the comparisons of polarization ellipses between the incident polarization states and the detected polarization states, respectively. The azimuth angle ψ in the polarization parameter can be extracted from the orientation angle ϑ of the transmitted x-polarization component. It can be observed that when axial ratios are less than one, the orientation angles ϑ are always along the x-direction. And orientation angles ϑ are always along the y-direction when axis ratios are greater than one. The ellipticity angle ε is extracted from the relative mode purity. The purity
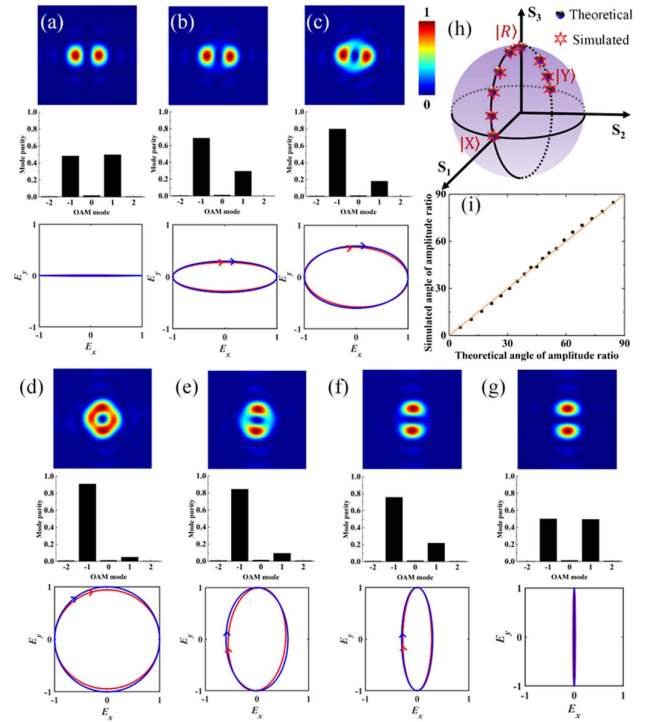

Fig. 3. Characterization of the proposed all-dielectric metasurface for polarization detection: the trajectory of the incident wave's polarization state follows the meridian direction, transitioning from x-polarization to right-handed circular polarization, and then to y-polarization. (a)–(g) Intensity distributions, mode purity spectra of the transmitted vortex fields, and comparisons of polarization ellipses between the incident polarization states (blue) and the detected polarization states (red). (h) Representation as points on the Poincaré sphere of the input states (spheres) and the corresponding states identified by the metasurface (hexagrams). (i) Comparison of theoretical angles of amplitude ratio and obtained angles through simulations.

spectra of each polarization state are shown in the second row of Figs. 3(a)–3(g). It can be seen that, under linearly polarized incidences, the mode purities of vortex fields with topological charges of $+1$ and -1 are almost the same. As the axial ratio gradually increases to one, the proportion of modes with a topological charge of -1 increases, corresponding to an increase in the right-handed circularly polarized component in the incident field. Detailed data of the orientation angles ϑ and mode purity spectra of each polarization state are in Table 1 (see Appendix B). The comparisons of polarization ellipses in the third row of Figs. 3(a)–3(g) and the points on the Poincaré sphere in Fig. 3(h) qualitatively show the difference between the detected and incident polarization states. The angle of amplitude ratio α is used to quantitatively compare the difference between incident and transmitted polarization states in Fig. 3(i). It can be seen that all the data points are around the line along the 45° direction.

As the second part, the trajectory of the incident wave's polarization state follows the equatorial direction, from $-45°$-linear polarization through x-polarization, and then to 45°-linear polarization. The incident polarization states on this trajectory can be set by changing the angle of amplitude ratio;
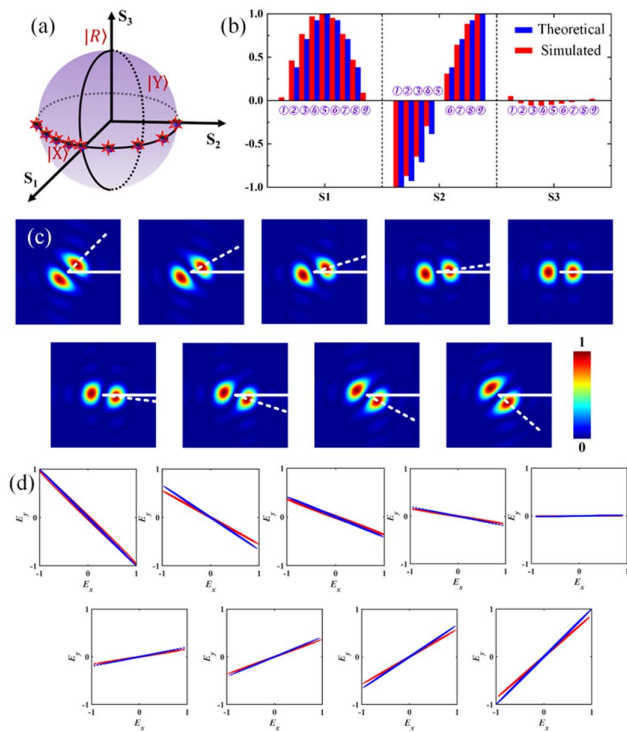
Fig. 4. Characterization of the proposed all-dielectric metasurface for polarization detection: the trajectory of the incident wave's polarization state follows the equatorial direction, from –45°-linear polarization through x-polarization, and then to 45°-linear polarization. (a) Representation as points on the Poincaré sphere of the input states (spheres) and the corresponding states identified by the metasurface (hexagrams). (b) Full-Stokes parameters of the incident polarization states and the corresponding states identified by the proposed metasurface. (c) Intensity distributions of the transmitted x-polarized field. (d) Polarization ellipses of the incident polarization states (blue) and the detected polarization states (red).

the selected angles are $-\pi/4$, $-3\pi/16$, $-\pi/8$, $-\pi/16$, 0, $\pi/16$, $\pi/8$, $\pi/16$, and $\pi/4$. The intensity distributions of the transmitted x-polarized field under different linearly polarized incidences are shown in Fig. 4(c). Their orientation rotates continuously clockwise as the incident polarization changes. The detailed orientation angles are listed in Table 2 (see Appendix C). The mode purity spectra of transmitted vortex fields under each linearly polarized incidence are also simulated, and detailed data are shown in Table 2. Using the calculated parameters of azimuth angle ψ and ellipticity angle ε, the other parameters, including angle of amplitude ratio α and phase difference δ, can be further calculated. The polarization ellipses of the incident polarization states and the detected polarization states are plotted in Fig. 4(d). The detected polarization states are generally consistent with the incident polarization states, except for a few slight angle deviations. The Poincaré sphere [Fig. 4(a)] and full-Stokes parameters [Fig. 4(b)] are also used to compare the differences between theoretical and simulated results. The Stokes parameter S_3 is essentially zero, indicating that the intensities of the left-handed and right-handed circularly polarized components in the transmitted field are almost the same. The simulated Stokes parameters S_1 and S_2, which

are used to characterize the intensity difference in linear polarizations, show slight discrepancies compared to the theoretical data.

In addition to selecting specific polarization states on certain trajectories in the previous two parts, the performance of the proposed metasurface in identifying arbitrary elliptical polarization states is also tested. Five arbitrarily selected elliptically polarized waves are incident on the proposed device, and then the incident polarization states are detected by analyzing the distributions of the transmitted field. The intensity distributions of the transmitted x-polarized field are shown in Fig. 5(a). Their orientation angles can be analyzed from these figures, which in turn provide the azimuth angles ψ. The corresponding phase distributions are shown in the insets, where the fifth phase profile exhibits opposite rotation compared to the others, indicating left-handedness. Then their ellipticity angles ε are calculated by analyzing the mode purities of the transmitted field. Detailed simulation data are recorded in Table 3 (see Appendix D). The polarization ellipses of the incident polarization states and the detected polarization states are shown in Fig. 5(b). They have the same rotation directions, except for slight deviations, and essentially have the same shapes. In addition, Poincaré spheres and full-Stokes parameters are used to characterize them. There are small shifts in their positions (marked as hexagram and ∗) on the Poincaré sphere. Their Stokes parameters have similar values.

In addition to the above simulations, one sample is fabricated for experimental characterization, using the standard ultraviolet lithography process and inductively coupled plasma etching techniques. The scanning electron microscopy (SEM) image is shown in Fig. 6(a), and the inset shows its side view. The sample contains 50×50 meta-atoms and the side
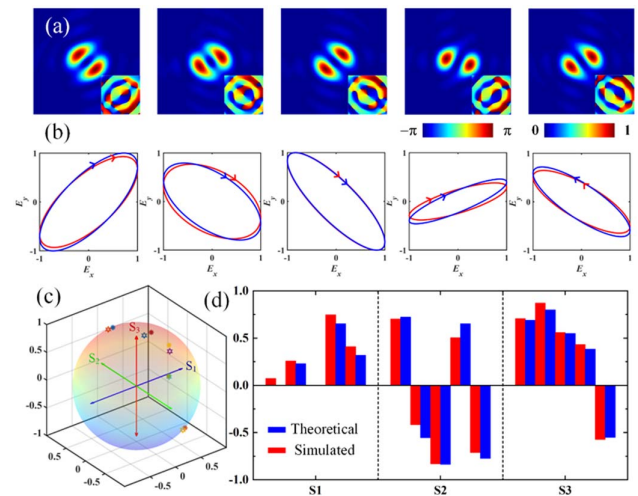

Fig. 5. Characterization of the proposed all-dielectric metasurface for polarization detection: five arbitrarily selected elliptical polarization states. (a) Intensity distributions of the transmitted x-polarized field. The insets are corresponding phase distributions. (b) Polarization ellipses of the incident polarization states and the detected polarization states. (c) Representation as points on the Poincaré sphere of the input states (hexagrams) and the corresponding states identified by the metasurface (∗). (d) Full-Stokes parameters of the incident polarization states and the corresponding states identified by the proposed metasurface.
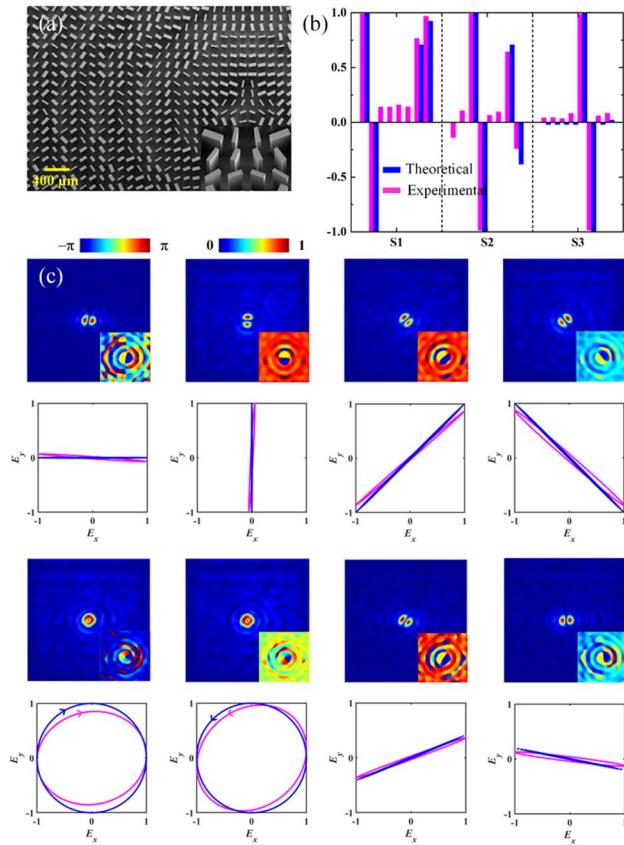
Fig. 6. Experimental characterization of the proposed all-dielectric metasurface for terahertz polarization detection. (a) SEM image of fabricated metasurface. The inset is a partially enlarged side view. (b) Full-Stokes parameters of the incident polarization states and the corresponding states experimentally identified by the proposed polarization detection scheme. (c) Intensity distributions, phase distributions, and comparisons of polarization ellipses between the incident polarization states (blue) and the measured polarization states (magenta).

and the blue ones are corresponding theoretical values. When the polarization state is x-polarization or y-polarization, Stokes parameter S_1 is $+1$ or -1, while the other two parameters are almost always zero. For the incident 45°-polarization or −45°-polarization, S_2 has a value of $+1$ or -1, while the other two are close to zero. When the incident wave is circularly polarized, S_3 takes the value of $+1$ or -1. Generally speaking, experimental results are in good agreement with the theoretical data.

4. CONCLUSION

In summary, we demonstrate a novel scheme for terahertz polarization detection using an all-dielectric metasurface. By performing mode purity analysis of the transmitted vortex field and conducting multidimensional analysis of the transmitted field, complete polarization parameters of the incident field are resolved. Polarization ellipses, Poincaré spheres, and full-Stokes parameters are used to reconstruct the polarization states of the incident wave. The power of the proposed metasurface in polarization recognition is verified by using three polarization trajectories, including linear polarizations, circular polarizations, and elliptical polarizations. The metasurface sample is fabricated, and the performance of polarization detection is characterized by experiments. The experimental results are in good agreement with the theoretical values, which indicates the potential of the metasurface in polarization detection. The proposal of this approach has played a significant role in the development of ultra-compact terahertz polarization detection devices, effectively advancing the application of terahertz technology.

APPENDIX A: TRANSMITTED FIELDS OF THE PROPOSED ALL-DIELECTRIC METASURFACE UNDER LEFT-HANDED AND RIGHT-HANDED CIRCULARLY POLARIZED INCIDENCES

length is 7.5 mm. A laboratory-built terahertz digital holographic imaging system is used to test the performance of the fabricated sample. The intensity distributions of the experimentally measured x-polarized components are shown in the first and third rows of Fig. 6(c). The incident polarization states are x-polarization, y-polarization, 45°-polarization, −45°-polarization, right-handed circular polarization, left-handed circular polarization, 22.5°-polarization, and −11.25°-polarization. The azimuth angles ψ are extracted from the intensity distributions of the x-polarized component, and the ellipticity angles ε are calculated from the total transmitted fields. These results are recorded in Table 4 (see Appendix E). For two circular polarizations of these states, their rotations can be extracted from the phase distributions of the x-polarized component, and they are right-handed and left-handed circular polarizations. The comparisons of polarization ellipses between the incident polarization states and the measured polarization states are shown in the second and fourth rows of Fig. 6(c). In addition, full-Stokes parameters of each polarization are compared in Fig. 6(b); magenta bars represent the measured results

Fig. 7. Transmitted fields of the proposed all-dielectric metasurface under left-handed and right-handed circularly polarized incidences. (a) Intensity distribution of the transmitted right-handed circularly polarized channel under left-handed circularly polarized incidence. The inset is corresponding phase distribution. (b) Intensity distribution of the transmitted left-handed circularly polarized channel under right-handed circularly polarized incidence. The inset is corresponding phase distribution.

APPENDIX B: SIMULATED ORIENTATION ANGLES ϑ AND MODE PURITY SPECTRA OF EACH POLARIZATION STATE OF THE FIRST TRAJECTORY

Table 1. Simulated Orientation Angles ϑ and Mode Purity Spectra of Each Polarization State of the First Trajectory

Polarization					*X*		
Axial ratio		0.1	0.2	0.3	0.4	0.5	0.6
Orientation angle ϑ (°)	0	0	0	0	179	178	177
Mode purity of −1	0.49	0.56	0.64	0.68	0.73	0.76	0.80
Mode purity of +1	0.48	0.40	0.34	0.29	0.25	0.21	0.18
Axial ratio	0.7	0.8	0.9	1	1/0.9	1/0.8	1/0.7
Orientation angle ϑ (°)	176	176	174	×	86	85	87
Mode purity of −1	0.83	0.86	0.88	0.92	0.91	0.90	0.88
Mode purity of +1	0.15	0.12	0.09	0.05	0.05	0.06	0.08
Polarization					*Y*		
Axial ratio	1/0.6	1/0.5	1/0.4	1/0.3	1/0.2	1/0.1	
Orientation angle ϑ (°)	87	88	89	89	90	90	90
Mode purity of −1	0.84	0.8	0.76	0.74	0.7	0.64	0.50
Mode purity of +1	0.10	0.13	0.17	0.22	0.27	0.34	0.49

APPENDIX C: SIMULATED ORIENTATION ANGLES ϑ AND MODE PURITY SPECTRA OF EACH POLARIZATION STATE OF THE SECOND TRAJECTORY

Table 2. Simulated Orientation Angles ϑ and Mode Purity Spectra of Each Polarization State of the Second Trajectory

Angle of amplitude ratio	$-\pi/4$	$-3\pi/16$	$-\pi/8$	$-\pi/16$	0
Orientation angle ϑ (°)	44	30	16	12	0
Mode purity of −1	0.50	0.47	0.46	0.46	0.47
Mode purity of +1	0.47	0.49	0.50	0.50	0.50
Angle of amplitude ratio		$\pi/16$	$\pi/8$	$3\pi/16$	$\pi/4$
Orientation angle ϑ (°)		170	160	150	140
Mode purity of −1		0.47	0.48	0.48	0.49
Mode purity of +1		0.49	0.49	0.48	0.48

APPENDIX D: SIMULATED ORIENTATION ANGLES ϑ AND MODE PURITY SPECTRA OF EACH POLARIZATION STATE OF THE THIRD TRAJECTORY

Table 3. Simulated Orientation Angles ϑ and Mode Purity Spectra of Each Polarization State of the Third Trajectory

Spin	Right	Right	Right	Right	Left
Axial ratio	0.4	0.5	0.3	0.2	0.3
Angle of amplitude ratio	$\pi/4$	$-3\pi/16$	$-\pi/4$	$\pi/8$	$-3\pi/16$
Orientation angle ϑ (°)	137	31	45	161	32
Mode purity of −1	0.77	0.79	0.76	0.65	0.21
Mode purity of +1	0.19	0.18	0.22	0.32	0.77

APPENDIX E: MEASURED ORIENTATION ANGLES ϑ AND MODE PURITY SPECTRA OF EACH POLARIZATION STATE

Table 4. Measured Orientation Angles ϑ and Mode Purity Spectra of Each Polarization State

Polarization	*X*	*Y*	45°	−45°
Orientation angle ϑ (°)	176	93	138	40
Mode purity of −1	0.34	0.34	0.32	0.46
Mode purity of +1	0.32	0.32	0.31	0.42
Polarization	RCP	LCP	22.5°	−11.25°
Orientation angle ϑ (°)	80	130	160	171
Mode purity of −1	0.74	0.04	0.36	0.39
Mode purity of +1	0.04	0.74	0.32	0.33

Disclosures. The authors declare no conflicts of interest.

Data Availability. Data underlying the results presented in this paper are not publicly available at this time but may be obtained from the authors upon reasonable request.

REFERENCES

1. N. Yu, P. Genevet, M. A. Kats, F. Aieta, J.-P. Tetienne, F. Capasso, and Z. Gaburro, "Light propagation with phase discontinuities: generalized laws of reflection and refraction," Science **334**, 333–337 (2011).
2. J. Ni, C. Huang, L.-M. Zhou, M. Gu, Q. Song, Y. Kivshar, and C.-W. Qiu, "Multidimensional phase singularities in nanophotonics," Science **374**, eabj0039 (2021).
3. H. Zhang, X. B. Sha, Q. M. Chen, J. P. Cheng, Z. H. Ji, Q. H. Song, S. H. Yu, and S. M. Xiao, "All-dielectric metasurface-enabled multiple vortex emissions," Adv. Mater. **34**, 2109255 (2022).
4. B. Wang, B. Quan, J. He, Z. Xie, X. Wang, J. Li, Q. Kan, and Y. Zhang, "Wavelength de-multiplexing metasurface hologram," Sci. Rep. **6**, 35657 (2016).
5. Z. Liu, S. Chen, J. Li, H. Cheng, Z. Li, W. Liu, P. Yu, J. Xia, and J. Tian, "Fully interferometric controllable anomalous refraction efficiency using cross modulation with plasmonic metasurfaces," Opt. Lett. **39**, 6763–6766 (2014).
6. Z. Yue, J. Liu, J. Li, J. Li, C. Zheng, G. Wang, M. Chen, H. Xu, Q. Wang, X. Xing, Y. Zhang, Y. Zhang, and J. Yao, "Multifunctional terahertz metasurfaces for polarization transformation and wavefront manipulation," Nanoscale **13**, 14490–14496 (2021).

7. A. H. Dorrah, N. A. Rubin, A. Zaidi, M. Tamagnone, and F. Capasso, "Metasurface optics for on-demand polarization transformations along the optical path," Nat. Photonics **15**, 287–296 (2021).

8. D. Hu, X. Wang, S. Feng, J. Ye, W. Sun, Q. Kan, P. J. Klar, and Y. Zhang, "Ultrathin terahertz planar elements," Adv. Opt. Mater. **1**, 186–191 (2013).

9. G. Zheng, H. Mühlenbernd, M. Kenney, G. Li, T. Zentgraf, and S. Zhang, "Metasurface holograms reaching 80% efficiency," Nat. Nanotechnol. **10**, 308–312 (2015).

10. X. Chen, M. Chen, M. Q. Mehmood, D. Wen, F. Yue, C. W. Qiu, and S. Zhang, "Longitudinal multifoci metalens for circularly polarized light," Adv. Opt. Mater. **3**, 1201–1206 (2015).

11. R. Wang, Y. Intaravanne, S. Li, J. Han, S. Chen, J. Liu, S. Zhang, L. Li, and X. Chen, "Metalens for generating a customized vectorial focal curve," Nano Lett. **21**, 2081–2087 (2021).

12. R. C. Devlin, A. Ambrosio, N. A. Rubin, J. P. B. Mueller, and F. Capasso, "Arbitrary spin-to-orbital angular momentum conversion of light," Science **358**, 896–901 (2017).

13. C. Zheng, J. Li, J. Li, Z. Yue, S. Wang, M. Li, H. Zhao, X. Hao, H. Zang, Y. Zhang, and J. Yao, "All-silicon chiral metasurfaces and wavefront shaping assisted by interference," Sci. China Phys. Mech. **64**, 114212 (2021).

14. C. L. Zheng, J. Li, J. Y. Liu, J. T. Li, Z. Yue, H. Li, F. Yang, Y. T. Zhang, Y. Zhang, and J. Q. Yao, "Creating longitudinally varying vector vortex beams with an all-dielectric metasurface," Laser Photon. Rev. **16**, 2200236 (2022).

15. S. Xiao, T. Wang, T. Liu, C. Zhou, X. Jiang, and J. Zhang, "Active metamaterials and metadevices: a review," J. Phys. D **53**, 503002 (2020).

16. T. Liu, Z. Han, J. Duan, and S. Xiao, "Phase-change metasurfaces for dynamic image display and information encryption," Phys. Rev. Appl. **18**, 044078 (2022).

17. Y. Shen, X. Wang, Z. Xie, C. Min, X. Fu, Q. Liu, M. Gong, and X. Yuan, "Optical vortices 30 years on: OAM manipulation from topological charge to multiple singularities," Light Sci. Appl. **8**, 90 (2019).

18. M. E. J. Friese, T. A. Nieminen, N. R. Heckenberg, and H. Rubinsztein-Dunlop, "Optical alignment and spinning of laser-trapped microscopic particles," Nature **394**, 348–350 (1998).

19. F. Yue, D. Wen, C. Zhang, B. D. Gerardot, W. Wang, S. Zhang, and X. Chen, "Multichannel polarization-controllable superpositions of orbital angular momentum states," Adv. Mater. **29**, 1603838 (2017).

20. M. W. Beijersbergen, L. Allen, H. E. L. O. van der Veen, and J. P. Woerdman, "Astigmatic laser mode converters and transfer of orbital angular momentum," Opt. Commun. **96**, 123–132 (1993).

21. L. Wei, Y. Gao, X. Wen, Z. Zhao, L. Cao, and Y. Gu, "Fractional spiral zone plates," J. Opt. Soc. Am. A **30**, 233–237 (2013).

22. Y. Yuan, S. Sun, Y. Chen, K. Zhang, X. Ding, B. Ratni, Q. Wu, S. N. Burokur, and C.-W. Qiu, "A fully phase-modulated metasurface as an energy-controllable circular polarization router," Adv. Sci. **7**, 2001437 (2020).

23. L. Marrucci, E. Karimi, S. Slussarenko, B. Piccirillo, E. Santamato, E. Nagali, and F. Sciarrino, "Spin-to-orbital conversion of the angular momentum of light and its classical and quantum applications," J. Opt. **13**, 064001 (2011).

24. H. Wu, Q. Zeng, X. Wang, C. Li, Z. Huang, Z. Xie, Y. He, J. Liu, H. Ye, Y. Chen, Y. Li, D. Fan, and S. Chen, "Polarization-dependent phase-modulation metasurface for vortex beam (de)multiplexing," Nanophotonics **12**, 1129–1135 (2023).

25. Y. X. Zhang, J. J. Jin, M. B. Pu, Q. He, Y. H. Guo, X. Li, X. L. Ma, and X. G. Luo, "Full stokes polarimetry for wide-angle incident light," Phys. Status Solidi RRL **14**, 2000044 (2020).

26. C. Zhang, J. Hu, Y. Dong, A. Zeng, H. Huang, and C. Wang, "High efficiency all-dielectric pixelated metasurface for near-infrared full-Stokes polarization detection," Photon. Res. **9**, 583–589 (2021).

27. Z. Jiang, J. H. Lu, J. Y. Fan, J. X. Liang, M. Zhang, H. Su, L. Zhang, and H. W. Liang, "Polarization-multiplexing bessel vortex beams for polarization detection of continuous terahertz waves," Laser Photon. Rev. **17**, 2200484 (2023).

28. J. P. Balthasar Mueller, N. A. Rubin, R. C. Devlin, B. Groever, and F. Capasso, "Metasurface polarization optics: independent phase control of arbitrary orthogonal states of polarization," Phys. Rev. Lett. **118**, 113901 (2017).

29. C. Zheng, G. Wang, J. Li, J. Li, S. Wang, H. Zhao, M. Li, Z. Yue, Y. Zhang, Y. Zhang, and J. Yao, "All-dielectric metasurface for manipulating the superpositions of orbital angular momentum via spin-decoupling," Adv. Opt. Mater. **9**, 2002007 (2021).